Nano Research

Open Access

Research Article

Synergistic effects of IL-3 release and Mn^{2+}-doped Prussian blue nanoparticles camouflaged with MES23.5 cell membranes on Alzheimer's disease therapy

Tuodi Zhang ✉, Zhonghui Xue, Qianqian He, Junling Yang, Ya Wen, Xiaohui Lu, Min Xu, and Yuehua Guo ✉

Research Center of Clinical Medicine, Affiliated Hospital of Nantong University, Nantong 226001, China

Cite this article: *Nano Research*, **2025**, *18*, 94907175. https://doi.org/10.26599/NR.2025.94907175

ABSTRACT: Alzheimer's disease (AD) is a progressive neurodegenerative disorder with prolonged latency during the prodromal stage. However, current clinical approaches to pharmacological interventions for AD remain challenge. An effective treatment strategy is to eliminate protein aggregates and prevent their regeneration. In this study, interleukin (IL)-3-loaded porous manganese (Mn^{2+})-doped Prussian blue (PB) nanoparticles (NPs) were coated with dopaminergic MES23.5 neuronal cell membranes (PBMn-IL3@CM) and then used to combat AD progression. The PBMn-IL3@CM NPs possessed a high targeting efficiency, being able to traverse the blood-brain barrier and specifically affect the brain to reduce oxidative stress. The Mn^{2+}-doped PB NPs effectively scavenged reactive oxygen radicals produced by microglia, inducing the pro-inflammatory M1 microglia. In addition, the released IL-3 activated microglia, causing the polarization of the M1 phenotype to the anti-inflammatory M2 phenotype *in vitro* and *in vivo*. The transition reduced phosphorylated tau accumulation, mediated neurotoxicity, and eliminated tau aggregates, which reversed cognitive impairment in AD mice. The PBMn-IL3@CM NPs showed excellent biocompatibility without significant adverse effects; consequently, they represent a promising AD treatment.

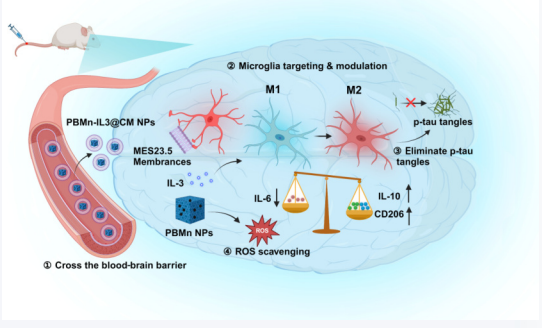

KEYWORDS: Alzheimer's disease, neuroinflammation, brain-targeted drug delivery, tau neuropathology, reactive oxygen species

1 Introduction

As life expectancy increases and the population ages, a growing number of people are developing neurodegenerative diseases [1]. Many typical biological processes are associated with this age-related class of neurodegenerative diseases, including protein misfolding, aggregation, and accumulation, as well as neuroinflammation, mitochondrial dysfunction, oxidative stress, autophagy dysregulation, and apoptosis [2–4]. Alzheimer's disease (AD) is the most prevalent of these diseases, affecting a significant portion of the population and ranking among the leading causes of death globally. The main pathological features of AD include the formation of fibrillar tangles containing intracellular phosphorylated tau (p-tau) protein and the deposition of amyloid beta (Aβ) in the brain [5, 6]. Despite extensive efforts to develop treatments, a cure for AD has remained elusive due to its complex pathogenesis. While much research has focused on Aβ, the failure of nearly all Aβ-targeting treatments in phase III clinical trials emphasizes the need to shift attention towards tau-targeted research [7–9]. Tau, a microtubule-associated protein crucial for regulating axonal microtubule stability, has emerged as a pivotal focus in AD research [10]. Additionally, another proposed pathological mechanism in which the liquid–liquid phase separation of tau protein contributes to the formation of amyloid fibrils, further highlights the significance of targeting p-tau as a therapeutic avenue for AD [11].

Microglia, innate immune cells situated in the brain, dynamically regulates their polarization to maintain brain homeostasis [12]. In AD, microglia release inflammatory mediators that influence the behaviors and functions of peripheral neurons, while glial cells lose their neuroprotective function and commence the aberrant phagocytosis of synapses and neurons [13, 14]. Additionally, microglia with an anti-inflammatory M2-like phenotype have the

Received: September 29, 2024; **Revised:** December 3, 2024
Accepted: December 5, 2024

✉Address correspondence to Tuodi Zhang, ntztd2022@163.com; Yuehua Guo, guoyuehuanju@163.com

capacity to concurrently phagocytose [15]. Two primary strategies in targeting microglia for AD therapy include addressing the inflammatory responses triggered by amyloid fibril accumulation in microglia and enhancing the efficiency of microglial clearance of amyloid fibril depositions [16]. Selecting optimal small molecules to activate microglia and eliminate protein accumulation is a valuable therapeutic strategy. Interleukin 3 (IL-3) is a cytokine with diverse roles in inflammation and autoimmune disorders. Astrocyte-derived IL-3 is instrumental in reprogramming microglia, thereby mitigating AD pathogenesis [17]. However, individual small molecule-based medications face challenges such as poor targeting and low absorption rates. Thus, the selection of an appropriate medication carrier is of utmost importance in developing effective AD treatments that target microglia.

In addition, AD can be aggravated by the excessive accumulation of protein tangles, leading to an increase in reactive oxygen radicals (ROS) in the brain [18]. The ROS, such as hydrogen peroxide (H_2O_2), superoxide anion, and hydroxyl radicals, can trigger mitochondrial dysfunction and cell death, contributing to the neurotoxicity associated with AD. Notably, ROS production can also have adverse effects on other tissues, including lipid peroxidation and DNA damage, which lead to tissue degradation and accelerated aging [19]. Elevated ROS levels can also induce M2 microglia to transition into the detrimental M1 phenotype [20]. Numerous nanomaterials, particularly nanozymes with peroxidase-like activities or catalase and superoxide dismutase-like activities, have been used to diagnose and treat AD [21, 22]. Prussian blue (PB), an antidote approved by the US Food and Drug Administration for treating poisoning by thallium and other radioactive elements [23], possesses unique characteristics when engineered into PB nanozymes (PBzymes). A PBzyme can effectively scavenge ROS [24, 25]. Although PB shows promise in mitigating ROS-induced damage and in potentially offering neuroprotection against AD, its effectiveness is hampered by poor penetration of the blood–brain barrier (BBB) and limited targeting. Recently, cell membrane-based biomimetic nanoparticles (NPs) emerged as a promising avenue for target therapy and imaging [26, 27]. These cell membrane-based NPs retain the physical and chemical properties of the NP core. This integration potentially endows the NPs with a wide range of desirable biological functions and makes them a promising tool for therapeutic and imaging applications.

Here, IL-3-loaded PBMn was constructed and coated with dopaminergic neuron (MES23.5) cell membranes (PBMn-IL3@CM) for AD treatment (Scheme 1). The strong binding affinity between VCAM-1 on the membrane of MES23.5 cells and $\alpha4\beta1$-integrin expressed on the surfaces of murine microglial BV-2 cells was attributed to the targeting capability of PBMn-IL3@CM and its high accumulation level in BV-2 cells. After injection through the tail vein, PBMn-IL3@CM traversed the BBB and targeted the brain specifically under the guidance of MES23.5 membranes. The PBMn NPs demonstrated an enzyme-like activity, effectively reducing ROS levels in the brain. Notably, the IL-3-based activation of microglia enhanced their capability to eliminate p-tau, prompting their polarization into neuroprotective M2-like cells that secreted anti-inflammatory cytokines and trophic factors. *In vitro* studies underscored the composite PBMn-IL3@CM NPs therapeutic potential, showcasing its ability to decrease p-tau levels, suppress ROS production, and reinforce neuroprotection against apoptosis. *In vivo* imaging findings corroborated the superior brain targeting of nanomaterials coated with MES23.5 neuronal cell membranes. Additionally, the PBMn-IL3@CM NPs treatment enhanced p-tau degradation, mitigated oxidative stress, reduced neuroinflammation, and alleviated neuropathy. This research represents a significant advancement in developing multifaceted and highly effective therapeutic strategies against tau-related neurodegenerative diseases.

2 Experimental

2.1 Materials

$K_3[Fe(CN)_6]$ and polyvinylpyrrolidone (PVP, K-30) were sourced from Sigma-Aldrich (St. Louis, MO, USA). Recombinant murine IL-3 was obtained from Protech (Woodinville, WA, USA). Potassium permanganate ($KMnO_4$) was purchased from Aladdin (Shanghai, China). The total superoxide dismutase (SOD) assay kit with WST-8, the Annexin V-FITC/PI assay kit, 3,3′-dioctadecyloxacarbocyanine perchlorate (DiO), the cell counting kit-8 (CCK-8), and the bicinchoninic acid (BCA) protein assay kit were

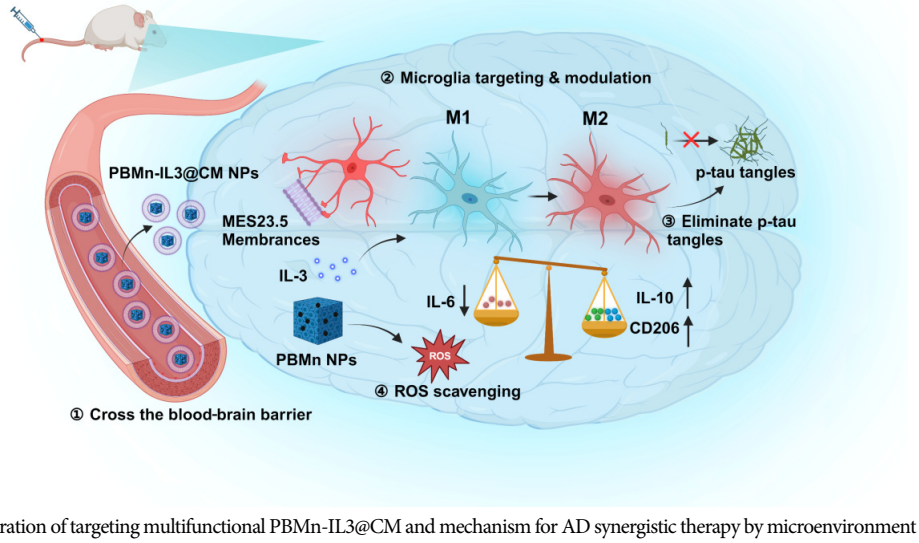

Scheme 1 Schematic illustration of targeting multifunctional PBMn-IL3@CM and mechanism for AD synergistic therapy by microenvironment remodeling.

sourced from Beyotime Biotechnology Co., Ltd. (Shanghai, China). Okadaic acid (OA) was obtained from Macklin (Shanghai, China). Dulbecco's modified Eagle's medium (DMEM), RPMI 1640 medium, fetal bovine serum (FBS), and trypsin-EDTA were obtained from Gibco (Thermo Fisher Scientific Inc., Waltham, MA, USA).

The mouse hippocampal neuronal cells (HT22), murine neonatal microglial BV-2 cells and dopaminergic neurons (MES23.5) were cultured in DMEM supplemented with 10% FBS, 1% penicillin, and 1% streptomycin at 37 °C in a 5% CO_2 incubator. PC12 cells were incubated with RPMI 1640 medium supplemented with 10% FBS, 1% penicillin, and 1% streptomycin. The Institute of Cancer Research (ICR) mice (6 weeks, male) were obtained from the Laboratory Animal Center of Nantong University. All the animals were housed under standard conditions, and the animal study protocols were approved by the Animal Care Committee of Nantong University (S20221118-003).

2.2 Synthesis of PBMn-IL3@CM

The PBMn-IL3@CM NPs were synthesized based on a previous report with minor modifications [28]. PVP-modified Mn-doped PB composite NPs were first synthesized using a hydrothermal method. In brief, 3 g PVP was dissolved in 80 mL of 0.01 M HCl solution. Then, $K_3[Fe(CN)_6]$ and $KMnO_4$ were added dropwise, resulting in the solution changing to brown over 30 min of stirring. The solution was further stirred and kept at 80 °C overnight to obtain PBMn. MES23.5 cell membranes were harvested as reported previously [17]. Subsequently, 1 mg/mL of PBMn NPs was diluted in PBS. The fusion of PBMn-IL3@CM NPs was achieved using ultrasound technology under hypothermic conditions. Specifically, PBMn and MES23.5 cell membrane fragments were mixed in PBS at a weight ratio of 1:1. Then, 0.5 μg/mL of IL-3 was added, and the mixture was sonicated for 5 min at a power of 100 W and a frequency of 42 kHz to obtain PBMn-IL3@CM NPs.

2.3 Characterization of synthesized NPs

The size and zeta potential of the synthesized NPs were characterized using a NanoBrook 90Plus (Malvern Nano, Malvern, UK). Ultraviolet–visible–near infrared (UV–vis–NIR) absorption spectra were recorded on a Shimadzu UV-2600 UV–Vis spectrophotometer. Fluorescence spectra were measured using a Shimadzu RF-6000 fluorescence spectrometer. The morphology was analyzed using transmission electron microscopy (TEM). Membrane proteins of MES23.5 cells were extracted using RIPA lysis buffer and quantified with a BCA protein assay kit. The identification of MES23.5 cell membrane proteins was performed using sodium dodecyl sulfate-polyacrylamide gel electrophoresis (SDS-PAGE).

2.4 ROS scavenging performance

First, the peroxidase (POD)-like activity was evaluated by measuring the distinctive absorption peak at 652 nm after catalyzing H_2O_2 to oxidize the substrate 3,5,3',5'-tetramethylbenzidine (TMB) [29]. Specifically, PBMn-related NPs at various concentrations (0, 0.1, 0.5, 1, 2, and 4 μg/mL) were added in 200 μL buffer solution containing 1% H_2O_2 and 1 mM TMB at room temperature. The absorbance of the color reaction at 652 nm was recorded using a microplate reader at 60-s intervals for 10 min. The superoxide anion scavenging ability of PBMn-related NPs was determined using a WST-8 SOD assay kit following the manufacturer's instructions. In brief, 160 μL of WST-8 working solution was added to 20 μL of PBMn-related NPs at different concentrations (0, 10, 20, 40, 60, and 80 μg/mL) and incubated at 37 °C for 30 min. The absorbance of the mixture was measured at 450 nm using a microplate reader. Catalase (CAT)-like activity was measured by non-fluorescent terephthalic acid (TA), which can be oxidized to produce fluorescent 2-hydroxyterephthalic acid with a fluorescence signal wavelength at 425 nm. PBMn-related NPs were incubated in 25 mM PBS (pH 7.4) at room temperature for 24 h. The fluorescence spectrum of the mixture was then measured at an excitation wavelength of 320 nm.

2.5 Cytotoxicity assay

BV-2, HT22, and PC12 cells (3×10^3 cells/well) were seeded into 96-well plates. After 24 h of incubation, the cells were treated independently with 0, 20, 50, 80, 100, 120, 150, 180, 200, and 220 nM OA to create pathological p-tau for the AD cell model. Subsequently, to evaluate the cytotoxicity, PB, PBMn, PBMn@CM, and PBMn-IL3@CM were each co-incubated with different cell lines at concentrations ranging from 0 to 100 μg/mL for an additional 24 h. Following this incubation period, the medium containing CCK-8 was replaced with 200 μL new medium per well, and the absorbance was measured at 450 nm.

2.6 Targeted validation of NPs

The BV-2 and HT22 cells were seeded at a density of 1×10^5 cells per 35 mm confocal dish (NEST, USA), respectively. Then, 1 mL of PBMn NPs, PBMn@CM NPs, and PBMn-IL3@CM NPs were mixed with DiO aqueous solution and stirred overnight at room temperature to obtain DiO-labeled NPs. Subsequently, BV-2 and HT22 cells were exposed to 10 μg/mL DiO-labeled PBMn NPs, PBMn@CM NPs, and PBMn-IL3@CM NPs independently for 2, 4, 6, 8, and 10 h. After sealing with an anti-fluorescence quencher containing 4',6-diamidino-2-phenylindole (DAPI), the cells were observed using confocal laser scanning microscopy (LSM900, Zeiss, USA).

2.7 Annexin V-FITC/PI double staining

HT22 cells were seeded in 6-well plates at a density of 3×10^5 cells per well and incubated for 24 h. Equal volumes of PBS, PBMn NPs, PBMn@CM NPs, and PBMn-IL3@CM NPs were added independently and incubated for an additional 24 h. After washing with PBS, trypsin was employed for cell detachment. Then, flow cytometry (FACSCanto, USA) was utilized to assess Annexin V-fluorescein isothiocyanate (FITC) (5 μL) and propidium iodide (PI) staining (5 μL) in accordance with the manufacturer's instructions.

2.8 CD206/CD86 staining

The BV-2 cells (1×10^5 cells per well) were seeded in a 6-well plate. After an additional 12 h of co-culturing with NPs, the cells were fixed, permeabilized, and blocked. Subsequently, the cells were incubated with FITC anti-mouse CD86 antibodies (Biolegend), or Alexa Fluor 647-conjugated CD206 antibodies (BD Pharmingen) at room temperature for 30 min in a dark environment. After washing with PBS, the cells were harvested, suspended in PBS, and analyzed using flow cytometry. The data analysis was performed using FlowJo software.

2.9 ROS detection *in vitro*

A 2',7'-dichlorodihydrofluorescein diacetate (DCFH-DA) probe was

used to track the generation of ROS. When DCFH-DA entered cells, it dissociated the acetyl group and became non-fluorescent DCFH. The intracellular ROS quickly oxidized the newly formed DCFH into 2',7'-dichlorofluorescein with bright fluorescence, which was proportionate to the ROS concentration [30]. In brief, HT22 cells were seeded in a 24-well plate at a density of 1×10^5 cells/well and cultured with OA (80 nM) for 24 h. Then, 10 μg/mL of PBMn, PBMn@CM, and PBMn-IL3@CM NPs were independently added and incubated for an additional 24 h. After washing, the cells were incubated in serum-free DMEM medium supplemented with 300 μL of DCFH-DA for 20 min. A subset of the cells was examined under an inverted fluorescence microscope (IX73, Olympus, China), and the fluorescence intensity was measured using flow cytometry.

2.10 Fluorescence imaging of NPs *in vivo*

DiO-labeled NPs were used to validate the NP accumulation and biodistribution in the brain. The ICR mice received a tail vein injection of 200 μL of DiO-labeled NPs at a concentration of 500 μg/mL. The mice were anesthetized and imaged using an *in vivo* imaging system at intervals of 0.5, 1, 2, 4, 8, and 24 h post injection. They were then sacrificed for the collection of major organs and *ex vivo* imaging.

2.11 Animal models and treatment

Male ICR mice (6 weeks old) were kept in a controlled environment with regulated temperature and humidity, following a 12-h day–night cycle, and they were provided with enough food and water. The ICR mice were anesthetized with 1.5% pentobarbital sodium (50 mg/kg) via intraperitoneal injection before being positioned in a stereotaxic apparatus. The OA (100 ng in 1 μL of saline) or saline (1 μL) was stereotaxically injected into the CA1 region of the right hippocampus at a coordinate of −2 mm anteroposterior (AP), −2 mm mediolateral (ML), and −2 mm dorsoventral (DV), according to the Mice Brain Paxinos Atlas [31]. Microinjection using a Hamilton stainless steel microsyringe was completed within 10 min. The needle was maintained in place for an additional 10 min to aid diffusion before being slowly removed over a 5-min period. The microinjection time for OA was set at Day 0. Tauopathy animal models have been considered successful at 6 days after microinjection [32, 33]. To validate the effectiveness of AD modeling, mice were randomly euthanized 1 week after obtaining the OA treatment, and the hippocampal proteins were collected for western blot verification. The mice were divided into five groups, each consisting of eight mice: a control group (saline), an AD group (OA + saline), and three therapy groups (OA + PBMn, OA + PBMn@CM, and OA + PBMn-IL3@CM). On the 6th day of OA modeling, mice received a tail vein injection of PBMn NPs, PBMn@CM NPs, PBMn-IL3@CM NPs, or saline. A second tail vein injection was administered 3 days later. On the 14th day, the Morris water maze (MWM) test was used to evaluate the spatial learning and memory functions of the mice.

2.12 Morris water maze test

The MWM test was conducted in a circular, blue opaque plastic maze situated within a soundproof, constant-light testing chamber. Prior to testing, the water was tinted with black nontoxic ink and maintained at a consistent depth of 20 cm. The maze tank was divided into four quadrants by two imaginary vertical lines crossing through the center: northwest, northeast, southwest, and southeast. During the training trial, a small platform was positioned in the center of the southwest quadrant. Its surface was 1 cm below the water surface, and it remained in place. The maze walls featured numerous stable visual cues. For 5 continuous days, each group conducted four acquisition trials per day. In each trial, the mouse's starting position was pseudorandomized to face the pool wall. The time necessary for each mouse to find the platform was recorded, and the escape was deemed successful. If the mouse takes longer than 90 s to reach the platform, it indicates failure and is kept there for an additional 15 s. The mice were dried with towels and absorbent paper. On the 6th day, the fixed platform was removed, and an exploration test was conducted to assess spatial memory. Each mouse was released into the water at the platform's farthest relative position and left to swim freely for 90 s. The performance of mouse latency, path length, and speed to locate and arrive on the platform were measured using EthoVision XT 16 software (Noldus Information Technology, Leesburg, VA, USA).

2.13 Western blotting

The hippocampal tissues were collected, and protein samples were obtained and lysed using phosphoprotein buffer, followed by centrifugation at 12,000 rpm for 10 min at 4 °C. The protein concentration was determined using the BCA kit in accordance with the manufacturer's instructions. Briefly, total proteins were separated using SDS-PAGE and subsequently transferred onto polyvinylidene fluoride (PVDF) membranes at 300 mA for 30 min. The membranes were then blocked with skimmed milk for 1 h and probed with p-tau primary antibodies overnight at 4 °C. They were then incubated with a horseradish peroxidase-conjugated secondary antibody at room temperature for 1 h. Finally, detection was performed using a chemiluminescence kit, and the bands were visualized and analyzed using an electrochemiluminescence (ECL) detection reagent.

2.14 Immunohistochemical staining

After being fixed in 4% paraformaldehyde for 24 h, the brain tissues (n = 8) were cleared in xylene, embedded in paraffin, and then cut into 5-μm slices. Afterwards, the paraffin sections were incubated with a recombinant anti-tau (phosphor S396) antibody (Abcam) at 4 °C overnight. Then, the slices were incubated using a four-color multiplex fluorescent immunohistochemistry kit (Absin) in accordance with the manufacturer's instructions. Anti-CD80 (eBioscience), CD206/MRC1 Mouse Monoclonal Antibody (Beyotime Biotechnology), anti-IL-6 (Proteintech), and anti-IL-10 (Proteintech) were incubated with the sections at 4 °C overnight. They were then incubated with goat anti-mouse (Abcam) at 37 °C for 1 h. Finally, an anti-fluorescence quenching mounting medium containing DAPI was used to stain the sections.

2.15 Hematoxylin and eosin staining

The brain hippocampal tissues were fixed with 10% formalin, embedded in paraffin, and sectioned at a thickness of 6 μm. Additionally, samples from the liver, spleen, lung, kidney, and brain were all mounted on slides and stained with hematoxylin and eosin (H&E). Subsequently, histological sections were examined using an optical microscope (DM3000, Leica, Germany).

2.16 Nissl staining

The samples underwent deparaffinization followed by rehydration.

Specifically, they were subjected to triple treatment with xylene, followed by a gradual hydration process involving ethanol gradients and deionized water. Subsequently, the samples were immersed in a 1% toluidine blue solution at 56 °C for 30 min and then thoroughly rinsed with double-distilled water until achieving a colorless state. Then, 95% ethanol was swiftly decomposed for a few seconds before samples were dehydrated and became translucent. This was followed by gradient dehydration with anhydrous ethanol, xylene removal, and finally sealing with neutral resin. The morphological characteristics of cortical neurons were examined using a Leica DM3000 optical microscope.

2.17 Statistical analysis

All the data are expressed as mean ± standard deviation (SD). Statistical comparisons between any two groups were calculated using either one-way ANOVAs or Student's t-tests. *P*-values < 0.05 were deemed statistically significant.

3 Results and discussion

3.1 Preparation and characterization of NPs

The route of the PBMn-IL3@CM synthesis is illustrated in Fig. 1(a). The addition of $KMnO_4$ under weak acidic conditions prompts Mn to form coordination bonds with the CN groups [34]. The hydrodynamic diameters of the established PBMn-IL3@CM NPs were 144.0 ± 0.3 nm (Fig. 1(b)), exhibiting remarkable colloidal stability (polydispersity index (PDI) = 0.170) as measured by dynamic light scattering. The PDI values of PB, PBMn, and PBMn@CM were 0.120, 0.244, and 0.245, respectively. The zeta

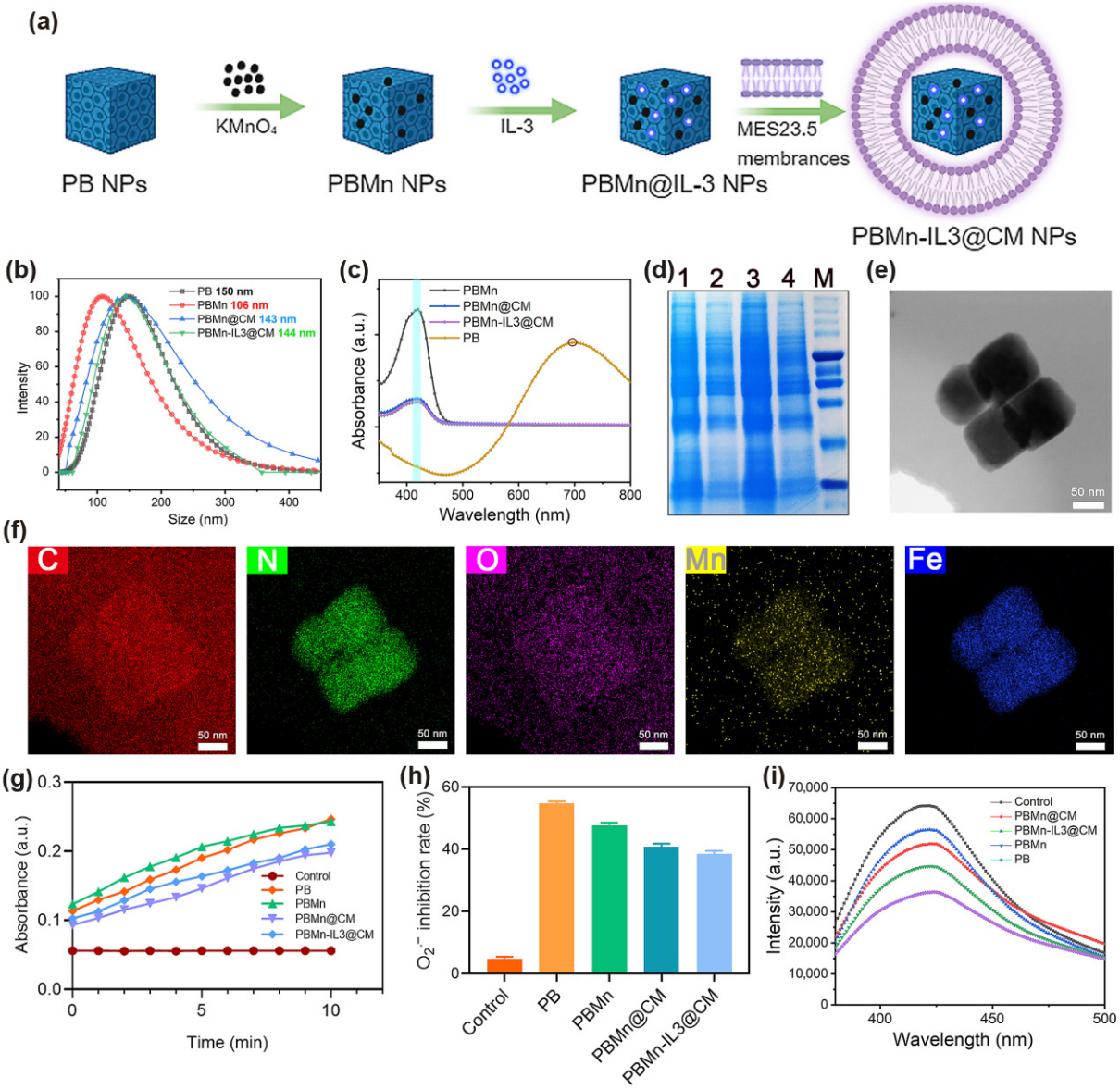

Figure 1 Characterization of PBMn-IL3@CM NP. (a) Schematic diagram of the preparation of PBMn-IL3@CM NP. (b) Size distributions of PB, PBMn, PBMn@CM, and PBMn-IL3@CM NPs. (c) UV–vis absorption spectra of PB, PBMn, PBMn@CM, and PBMn-IL3@CM NPs. (d) Protein profiles of a (1) MES23.5 cell membrane, (2) PBMn-IL3@CM membrane, (3) MES23.5 cell lysate, and (4) PBMn@CM. (e) TEM images of PBMn-IL3@CM NP. (f) TEM-EDS mapping of C, N, O, Fe, and Mn elements for PBMn-IL3@CM NP. (g) POD-like activities of PBMn-related NPs. (h) Effects of PBMn-related NPs on superoxide anions produced by xanthine oxidase. (i) CAT-like activities assessed by detecting oxygen generation from H_2O_2.

potentials of PB and PBMn NPs were −16.33 and −29.33 mV, respectively, which decreased to −38.2 mV after MES23.5 membrane loading and increased after IL-3 addition (Fig. S1 in the Electronic Supplementary Material (ESM)). The significant change in zeta potential indicated that PBMn-IL3@CM was successfully prepared.

The optical properties of the PBMn-related NPs were thoroughly investigated. The PB NPs demonstrated a broad absorption band from 500 to 900 nm, with a prominent absorption peak at 704 nm, which corresponded to the energy of the metal-to-metal charge transfer between Fe^{2+} and Fe^{3+} across the cyanide bridge [35]. Interestingly, upon introducing Mn^{2+} into PB nanocubes, the absorbance peak was visibly blue-shifted to approximately 400 nm (Fig. 1(c)). The presence of Mn^{2+} in the lattice may induce changes in the electron density and orbital energies of the cyanide bonds, which could account for the blue-shift [36, 37]. SDS-PAGE was used to investigate the protein profiles of the MES23.5 cell membrane (Fig. 1(d)). The similar protein profiles of PBMn-IL3@CM NPs, PBMn@CM, MES23.5 cell lysates, and the MES23.5 cell membrane demonstrate that PBMn and PBMn-IL3 were successfully coated with MES23.5 cell membranes. TEM was utilized to observe the morphologies of the NPs (Fig. 1(e) and Fig. S2 in the ESM). The PBMn-IL3 was a well-defined, uniform cuboidal structure, and limited changes were observed after surface modification with MES23.5 cell membranes. Furthermore, an elemental analysis confirmed the presence of typical Fe and Mn elements, further validating the successful synthesis of these NPs (Fig. 1(f)).

Excessive ROS production during oxidative stress can lead to protein, lipid, and DNA damage, which contribute to tissue damage [38]. In this study, the antioxidant-like properties of three formulas of PB-contained nanocarriers were investigated, including the activities of POD, SOD, and CAT. The absorbance gradually increased and was directly proportional to the PB, PBMn, PBMn@CM, and PBMn-IL3@CM levels (Fig. 1(g)), indicating that these NPs had good POD-like activities, with PBMn showing the highest POD activity. This may have been due to the generation of Mn oxides having antioxidant activities during PBMn synthesis [39]. Second, the formation of formazan from superoxide anions was detected at 450 nm to evaluate the SOD-like activities [40, 41]. PBMn NPs surpassed PB NPs in superoxide anion scavenging, as illustrated in Fig. 1(h), suggesting that Mn^{2+} doping improved superoxide anion scavenging capabilities. Finally, the dissolved oxygen produced by the PBMn-related NP-catalyzed breakdown of H_2O_2 was measured to evaluate CAT-like activities [42]. The increase in soluble oxygen compared with in the control suggested that PBMn-related NPs effectively accelerate the breakdown of H_2O_2, resulting in oxygen production (Fig. 1(i)). These findings confirmed the remarkable antioxidase-like properties of PBMn-related NPs, making PBMn-IL3@CM nanoagents promising candidates for ROS scavenging.

3.2 Biocompatibility and OA-induced p-tau *in vitro*

OA is a potent and selective inhibitor of protein phosphatase, which has been widely used to induce tau-related AD pathogenesis, including tau hyperphosphorylation and neuronal death [43, 44]. Herein, OA-induced HT22, BV-2, and PC12 cells have been used to establish tauopathy-like cell models. The cell viability decreased to approximately 55% when the OA concentration reached 80 nM, indicating significant neuronal death would occur at higher concentrations (Fig. 2(a), Figs. S3(a) and S4(a) in the ESM). Furthermore, the biocompatibility of PBMn-related NPs was evaluated. PBMn-related NPs in the range of 0–100 μg/mL did not exhibit significant cytotoxicity against HT22, BV-2, and PC12 cells (Fig. 2(b), Figs. S3(b) and S4(b) in the ESM). Subsequently, OA-induced cells were rescued by PBMn-related nanomaterials, and cell viability was displayed in Fig. 2(c). Compared with the OA group, the cell viability levels of HT22, BV-2, and PC12 increased after treating with PBMn-related NPs (Fig. S5 in the ESM).

The rescue effect of PBMn-related NPs on HT22 cells induced by OA was investigated using immunofluorescence. As shown in Fig. 2(d), a large amount of bright green fluorescence was observed after the addition of OA, demonstrating the up-regulated expression of p-tau. In addition, negligible fluorescence was observed from HT22 cells treated with PBMn-related NPs. The green fluorescence signal gradually increased along with the OA treatment time, peaking at 24 h (Fig. S6 in the ESM). The p-tau production in PC12 cells showed similar trends (Fig. S7 in the ESM). The down-regulation of p-tau levels was primarily attributed to the compensatory response caused by ROS removal [45]. These results verified the successful establishment of AD models at the cellular level. The findings also demonstrated that the synthesized PBMn-IL3@CM could reduce p-tau levels and maintain neuronal cell viability.

3.3 Biocompatibility and OA-induced p-tau *in vitro*

To demonstrate the targeting ability and specificity of PBMn-IL3@CM NPs, DiO-labeled PBMn-IL3@CM were incubated with BV-2 and HT22 cells for 2, 4, 6, 8, or 10 h, and the cellular uptake behavior was observed using confocal microscopy. As shown in Figs. 3(a)–3(f), the green fluorescence intensity was increased as the incubation time increased from 2 to 10 h, indicating substantial amounts of PBMn-IL3@CM were engulfed by BV-2 cells. The cellular uptake efficiency of PBMn-IL3@CM with HT22 cells was performed to investigate the targeting ability of PBMn-IL3@CM and only a weak fluorescence signal was observed even after 10 h incubation.

3.4 ROS scavenging and neuroprotective effect of PBMn-related NPs

The intracellular ROS scavenging ability of PBMn-related nanoparticles was investigated by fluorescence microscope and flow cytometry analyses. As shown in Fig. 4(a), the OA treatment induced a significant red fluorescence signal in HT22 cells, indicating high ROS levels. However, in the presence of PBMn-related NPs, the OA-treated HT22 cells displayed only a neglectable fluorescence intensity due to the scavenging effects of PBMn-related NPs on ROS. Flow cytometry also demonstrated that the fluorescence intensity of the OA-treated HT22 cells was significantly higher than those of the PBMn-related NP-treated groups, indicating the ROS scavenging ability of PBMn-related NPs (Fig. 4(b) and Fig. S8 in the ESM).

The inhibitory effects of PBMn-related NPs on the apoptosis of HT22 cells was evaluated using an Annexin V-FITC apoptosis detection kit. Consistent with the CCK-8 results, the data demonstrated robust salvaging effects for the NPs. The total apoptotic rates of the PBMn-, PBMn@CM-, and PBMn-IL3@CM-treated groups were 20.82%, 15.26%, and 8.12%, respectively, whereas the OA-treated group had a total apoptotic rate of 50.74%. The lowest apoptotic rate of the PBMn-IL3@CM group indicated a good therapeutic effect (Fig. 4(c)). The polarization effects of PBMn-

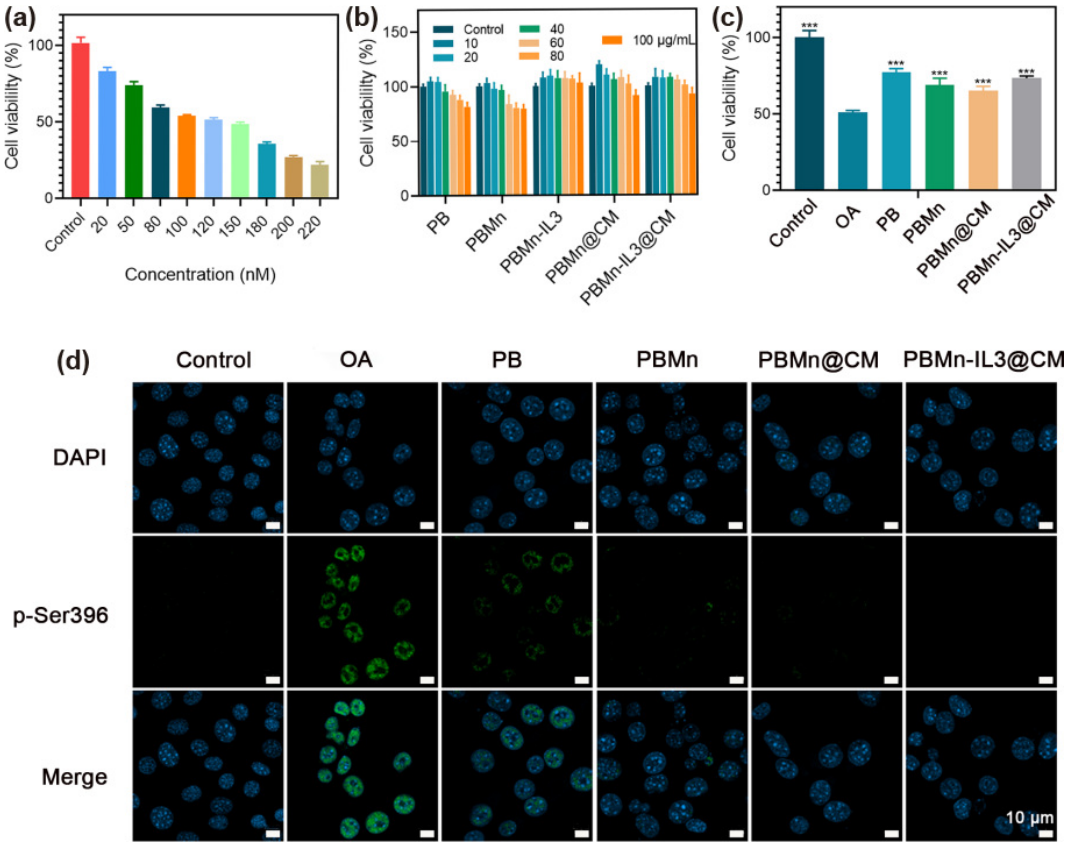

Figure 2 *In vitro* cell viability of HT22 after incubation 24 h with (a) OA, (b) PBMn-related NPs, and (c) OA + PBMn-related NPs at different concentrations. $^{*}P < 0.05$, $^{**}P < 0.01$, and $^{***}P < 0.001$ ($n = 6$). (d) Confocal fluorescence images of HT22 cells after exposure to 80 nM OA and then treated with PB, PBMn, PBMn@CM, and PBMn-IL3@CM NPs, independently. Blue: DAPI; green: pS396-Tau. Scale bars: 10 μm.

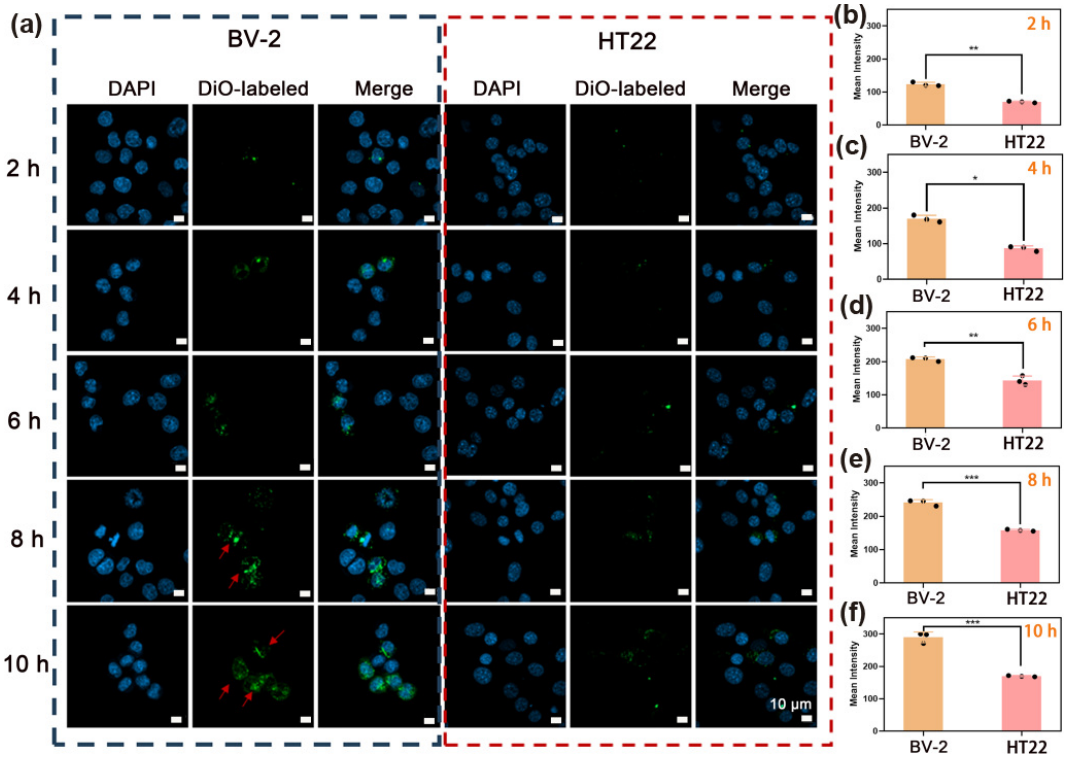

Figure 3 Targeting and specificity of PBMn-IL3@CM. (a) Confocal fluorescence images of BV-2 and HT22 cells treated with PBMn-IL3@CM NPs. Blue: DAPI; green: DiO-labeled PBMn-IL3@CM. Scale bars: 10 μm. Corresponding mean intensities of DiO-labeled PBMn-IL3@CM NPs at (b) 2, (c) 4, (d) 6, (e) 8, and (f) 10 h from (a). Data are presented as means ± SD ($n = 3$). $^{*}P < 0.05$, $^{**}P < 0.01$, and $^{***}P < 0.001$.

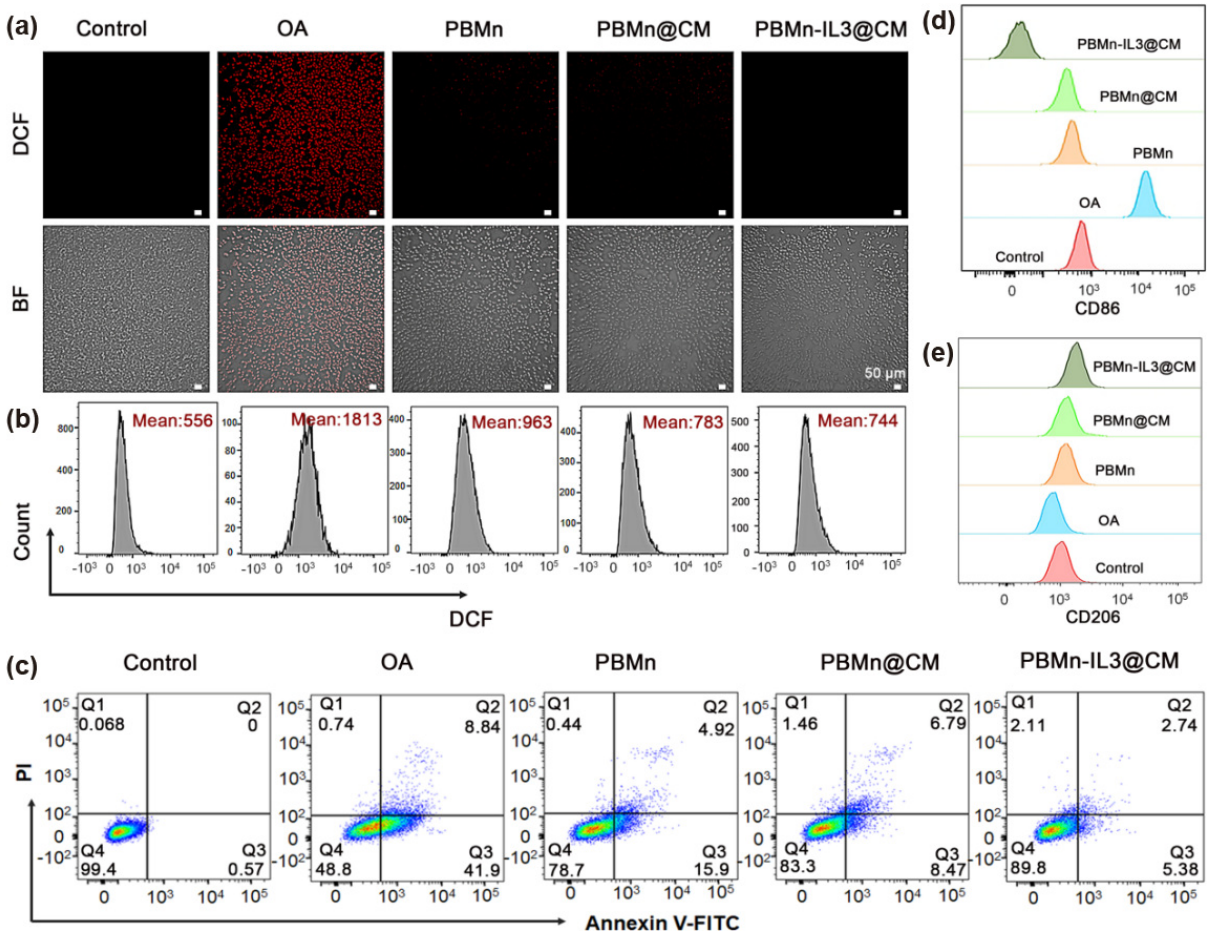

Figure 4 ROS scavenging and neuroprotective effect of PBMn-related NPs. (a) Fluorescence and bright-field images of HT22 cells after being exposed to 80 nM OA and then treated with PBMn NPs, PBMn@CM NPs, and PBMn-IL3@CM NPs, respectively. Scale bars: 50 μm. (b) Corresponding flow cytometry analysis of cellular ROS by DCFH-DA staining after different treatments. (c) Flow cytometry results for microglia BV-2 cell apoptosis by Annexin V-FITC/PI staining after different treatments. (d) Flow cytometry results of microglia BV-2 cells for CD86 expression after different treatments. (e) Flow cytometry results for CD206 expression after different treatments.

related NPs on BV-2 cells were evaluated by detecting CD86 (M1 marker) and CD206 (M2 marker). As demonstrated in Figs. 4(d) and 4(e), the OA treatment increased the CD86 expression level, causing the cells to exhibit pro-inflammatory effects, whereas rescue by PBMn-related NPs increased the CD206 expression level. This suggested that the pro-inflammatory M1 microglia can be modulated into anti-inflammatory M2 microglia by PBMn-IL3@CM. Thus, PBMn-related NPs, especially PBMn-IL3@CM, can rescue neurons from tauopathy-induced apoptosis by clearing p-tau and decreasing oxidative stress.

3.5 *In vivo* brain targeting of PBMn-IL3@CM

Before evaluating the therapeutic potential of PBMn-IL3@CM, its brain targeting ability was first assessed. The DiO-labeled PBMn-related NPs were injected into mice via the tail vein and photographed using an *in vivo* imaging system (IVIS) spectral system at 0.5, 1, 2, 4, 6, and 8 h. As shown in Fig. 5(a), MES23.5 membrane-coated PBMn group showed the highest fluorescence intensity and reached saturation at 2 h after injection. In addition, the PBMn@CM and PBMn-IL3@CM groups exhibited stronger fluorescence levels at every time point compared with other groups, suggesting that MES23.5 membrane-modified NPs have excellent brain targeting capacities. The tissue distribution further confirmed that the MES23.5 membrane-coated NPs accumulated in brains (Fig. 5(b)). These findings indicate that the MES23.5 payload provides active targeting of NPs to the brain.

3.6 Therapeutic evaluation of PBMn-IL3@CM in AD mice

The MWM experiment was employed to assess spatial memory and learning abilities of AD mice. As shown in Fig. 6(a), OA was administered into the CA1 region of the mouse hippocampus via a stereotaxic apparatus to establish the AD mouse model. This region plays a crucial role in the formation, consolidation, and retrieval of hippocampus-dependent memories [46]. Western blot analysis of hippocampal tissue showed that, the expression of p-tau in hippocampal tissue was significant increased after OA injection, indicating the successful establishment of AD mice model (Fig. S9 in the ESM).

During the learning acquisition phase, AD mice spent more time searching for the hidden platform compared to mice in the control and PBMn-related groups, indicating significant impairment in learning ability due to OA (Fig. S10(a) in the ESM). However, the escape latency of AD mice treated with PBMn@CM or PBMn-IL3@CM significantly improved during the 5-day spatial learning period, even though their swimming speed did not increase (Figs. S10(b) and S10(c) in the ESM). Similarly, during the spatial exploration phase, the saline treatment group displayed obvious learning deficits, while treated with PBMn@CM or PBMn-

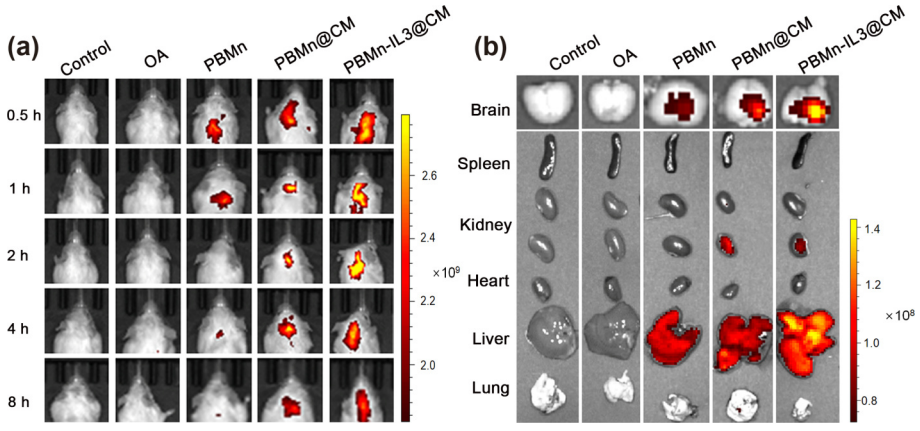

Figure 5 *In vivo* distribution. (a) Living imaging of OA-injected AD mice after intravenously injection with different formulations at different time. (b) *Ex vivo* imaging of tissues in each group after injection 24 h.

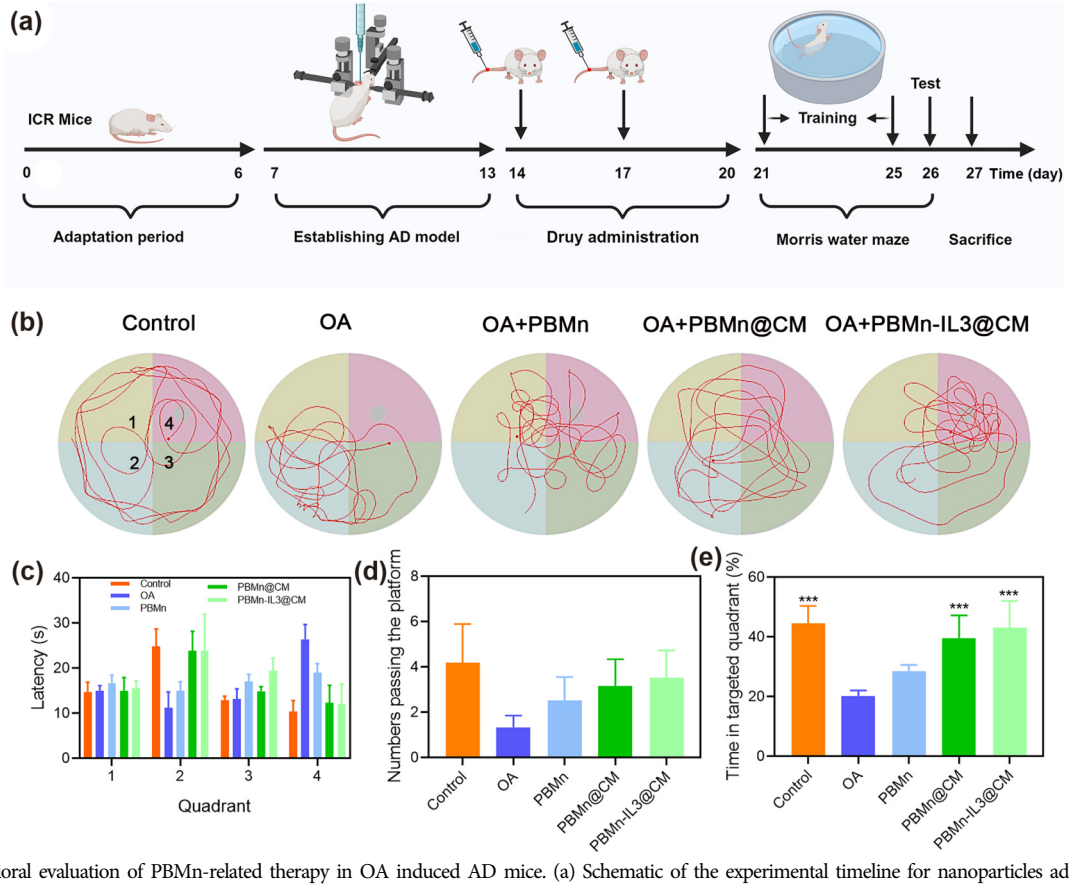

Figure 6 Behavioral evaluation of PBMn-related therapy in OA induced AD mice. (a) Schematic of the experimental timeline for nanoparticles administration and therapeutic evaluation. (b) Representative swimming trajectory of mice in MWM after different treatments. Labels 1, 2, and 3 indicate northwest, southwest, and southeast, respectively, whereas label 4 indicates the target quadrant (northeast) in the acquisition training trials. (c) Escape latency at different quadrant after different treatments. (d) The number of crossing the platform. (e) Ratio of time spent in target quadrant. Data were presented as mean ± SD, $n = 8$. One-way ANOVA, $^{*}P < 0.05$, $^{**}P < 0.01$, $^{***}P < 0.001$.

IL3@CM, the number of platform crossings and ratio of time in the target quadrant were sensibly ameliorated (Fig. 6(b)). Notably, the PBMn-IL3@CM treatment group's mice exhibited a considerable reduction in escape latency and the shortest search time on the platform (Fig. 6(c)), indicating a combined effect on increasing learning ability. Compared with PBMn or PBMn@CM NPs treatment alone, the PBMn-IL3@CM treatment dramatically enhanced the time spent in the target quadrant and the frequency of crossing platform positions (Figs. 6(d) and 6(e)). Finally, a western blot revealed that the PBMn-IL3@CM group showed a discernible decrease in the p-tau level after treatment (Fig. S11 in the ESM). These results suggested that PBMn-IL3@CM effectively restored the cognitive abilities of AD mice that were previously impaired by tauopathy.

3.7 P-tau clearance and neuroprotection *in vivo*

Immunofluorescence was used initially to assess the localization of PBMn-IL3@CM in mouse brains. The DiO-labeled PBMn@CM or

PBMn-IL3@CM NPs co-localized with p-tau, suggesting that the cell membrane-modified NPs accumulated in the hippocampus and cortex of the mouse brain (Fig. 7(a)). The OA group displayed the strongest red fluorescence, whereas the PBMn group displayed a visible reduction. Both the PBMn@CM and PBMn-IL3@CM groups showed almost no red fluorescence (Fig. 7(a) and Fig. S12 in the ESM). These results further indicated that cell membrane-modified NPs can penetrate the BBB and accumulate in the brain, which is crucial for AD therapy.

Nissl staining was used to observe the morphology, number, and distribution of Nissl bodies in neurons. The Nissl staining-based analysis of neuronal apoptosis in the CA1 and CA3 hippocampal regions of AD mouse brains revealed that PBMn-related NPs enhanced neuronal survival after OA treatments (Fig. 7(b)). Compared with in the control group, the Nissl bodies in most of the cells were dissipated and the staining appeared lighter in the CA1 and CA3 regions in OA-treated mouse groups. In addition, neuronal shrinkage or disappearance in brain tissues was observed in the OA group. This improved after treatment with PBMn-IL3@CM, particularly in the CA3 region, and PBMn@CM treatment group showed almost the same result. The improvement observed with the derivatives was significant compared with treatment with OA alone (Fig. 7(b)). Therefore, we hypothesized that PBMn-IL3@CM helped improve neuronal survival and reduce neuronal damage.

3.8 PBMn-IL3@CM reduces neuroinflammation in AD mice

Polarizing M1-type microglia to the anti-inflammatory M2-like phenotype has significant potential for normalizing the brain microenvironment [47]. The polarization effects of PBMn-IL3@CM on microglia were investigated by staining brain sections with CD80/CD206 (Fig. 8). Notably, strong CD80-positive orange fluorescence was observed in the hippocampus and cortex regions of AD mice compared with in the control group. The fluorescence intensity diminished notably after treatment with various NPs, particularly the PBMn-IL3@CM group, indicating the synergistic effect of PBMn and IL-3. In contrast, the level of CD206 obviously increased after PBMn-related NP treatments. The PBMn-IL3@CM group showed the highest CD206 fluorescence intensity, indicating that the PBMn-IL3@CM treatment can successfully induce microglial polarization from the M1 to M2 phenotype in AD mouse brains, which was consistent with the *in vitro* cellular experimental results.

Pro-inflammatory cytokine levels were also detected, as shown in Fig. 8. The expression of the cytokine IL-6 significantly increased

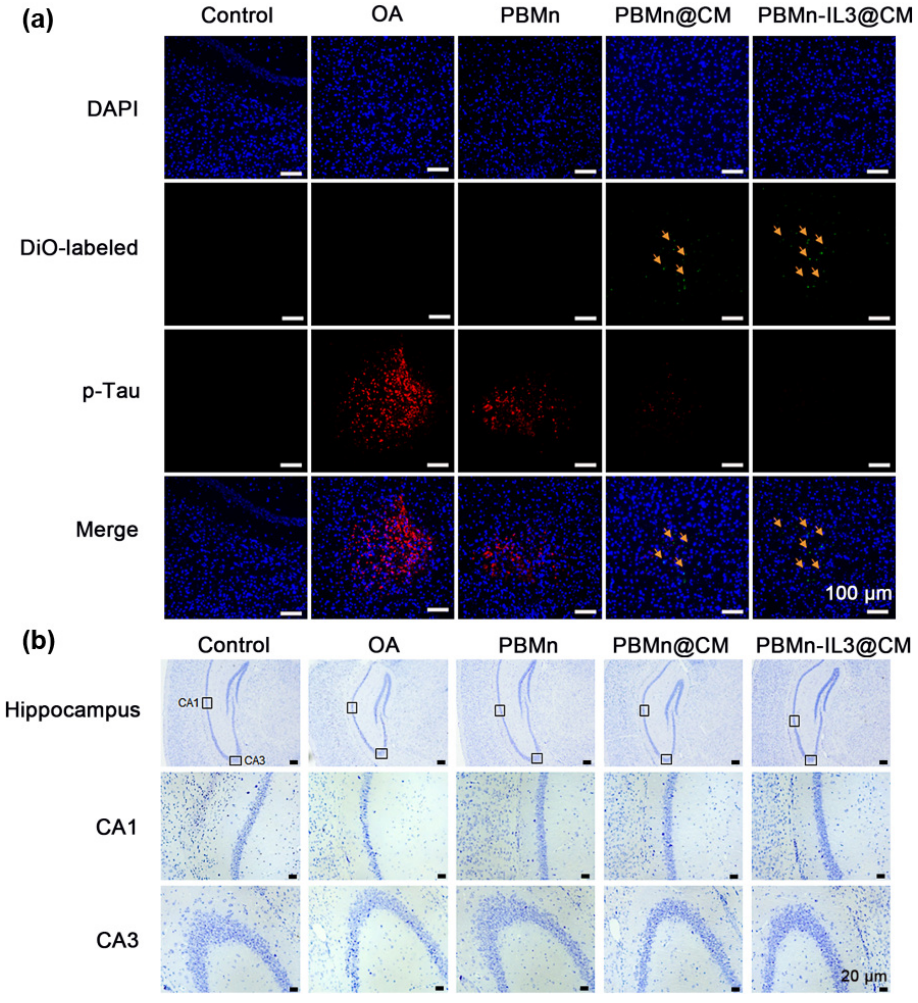

Figure 7 Investigation of p-tau clearance and neuroprotection. (a) Co-localization of DiO-labeled NPs and p-tau in hippocampus and cortex regions after different treatments. Green: DiO-labeled PBMn-related nanoparticles, red: p-tau, and blue represents DAPI. Scar bars: 100 μm. (b) Representative images of Nissl staining in the hippocampus and CA1, CA3 areas, scale bars: 20 μm.

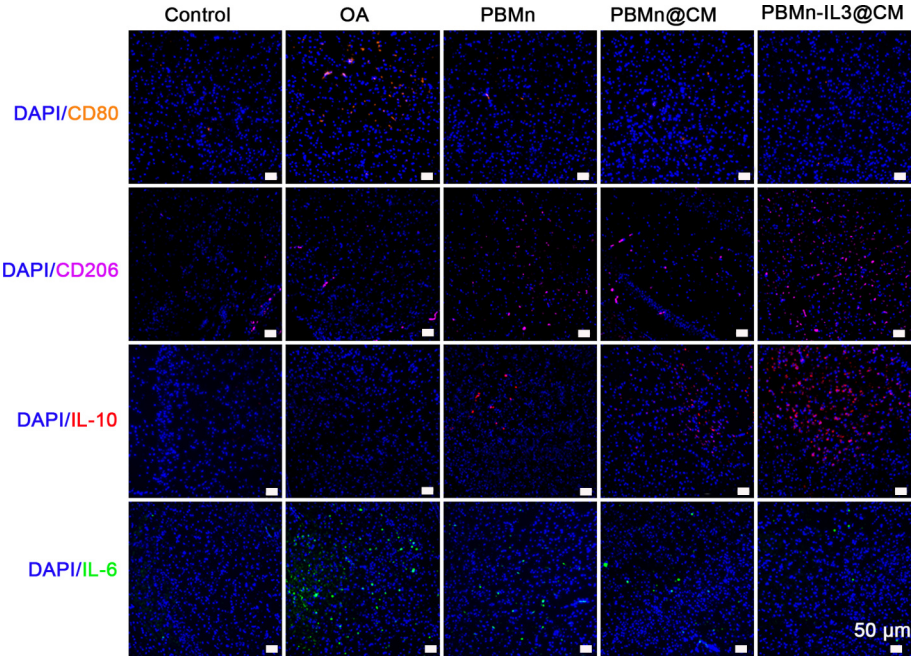

Figure 8 Immunofluorescence staining images of AD mouse brains after PBMn-related NPs treatment-induced microglial activation and regulated neuroinflammation. Fluorescence microscopy images from the first to the fourth rows show immunostaining of the M1 biomarker CD80, the M2 biomarker CD206, anti-inflammatory factor IL-10, and pro-inflammatory factor IL-6, respectively. Scale bars: 50 μm.

along with the p-tau level, but it significantly decreased after treatment with PBMn-related NPs (Fig. 8, as shown in the third and fourth rows). Conversely, in the OA-induced AD model group, anti-inflammatory IL-10 expression was markedly down-regulated because of elevated p-tau levels; however, its expression was up-regulated following treatment with distinct NP groups. Thus, PBMn-related NPs, through the introduction of IL-3 and its superior antioxidant properties, may change microglia from the inflammatory M1 phenotype to the anti-inflammatory M2 phenotype. The combined effects of activated microglial phenotypic polarization and ROS scavenging could produce a promising AD treatment strategy.

3.9 *In vivo* biocompatibility

The H&E staining revealed no pathological alterations in vital organs, such as the heart, liver, spleen, lung, and kidney (Fig. S13 in the ESM). The results demonstrated that PBMn-IL3@CM have excellent tolerability and biosafety *in vivo*.

4 Conclusions

In conclusion, an IL-3-loaded porous Mn^{2+}-doped PB NP was developed and then coated with MES23.5 cell membranes. It was used as a potential AD treatment in a mouse model. The MES23.5 cell membranes coated on PBMn-IL3 effectively improved the ability of NPs to cross the BBB and accumulate in AD-affected brain regions. Furthermore, the released IL-3 could switch the inflammatory M1 microglial phenotype to the anti-inflammatory M2 phenotype. The scavenging of ROS by PBMn further enhanced the polarization of microglia from M1 to M2. The polarization to the M2 phenotype induced an increase in the neuroprotective cytokine IL-10 level and a decrease in the neurotoxic IL-6 level, resulting in anti-inflammatory effects. Furthermore, PBMn-IL3@CM demonstrated an outstanding efficacy in counteracting cognitive impairments and neurological damage in OA-induced AD mice, as well as in disrupting the damaging cycle of "p-tau aggregates–microglia polarization–ROS" in the AD brain microenvironment. These results highlight the potential use of PBMn-IL3@CM NPs in AD treatment, and provide a promising avenue for the treatment of other tauopathies or neurodegenerative disorders.

Electronic Supplementary Material: Supplementary material (zeta potential and TEM results of NPs, cell viability of BV-2 and PC12 cells, confocal fluorescence images of HT22 and PC12 cells, western blotting analysis of OA-induced AD model, Morris water maze assay of AD mice after therapy, immunofluorescence staining of p-tau aggregates, and H&E staining of brain, heart, liver, spleen, lung, and kidney) is available in the online version of this article at https://doi.org/10.26599/NR.2025.94907175.

Data availability

Additional data related to this paper may be requested from the corresponding author upon request.

Acknowledgements

This work was supported by Jiangsu Provincial Research Hospital (No. YJXYY202204) and Science and Technology Project of Nantong City (No. MS2023006).

Declaration of competing interest

All the contributing authors report no conflict of interests in this work.

Author contribution statement

T. D. Z.: Writing – original draft, methodology, investigation, data curation. Z. H. X.: Methodology, investigation. Q. Q. H.: Data

curation. J. L. Y.: Visualization, methodology. Y. W.: Methodology, investigation. X. H. L.: Resources. M. X.: Methodology. Y. H. G.: Writing – review & editing, investigation, funding acquisition, formal analysis, conceptualization.

Informed consent

None.

Ethics statement

The animal experiments were carried out following the guidelines of Animal Care Committee of the Nantong University (No. S20221118-003).

Use of AI statement

None.

References

[1] Hung, C. W.; Chen, Y. C.; Hsieh, W. L.; Chiou, S. H.; Kao, C. L. Ageing and neurodegenerative diseases. *Ageing Res. Rev.* **2010**, *9 suppl*, S36–S46

[2] Mistretta, M.; Farini, A.; Torrente, Y.; Villa, C. Multifaceted nanoparticles: Emerging mechanisms and therapies in neurodegenerative diseases. *Brain* **2023**, *146*, 2227–2240.

[3] Ge, K. Z.; Li, Z.; Wang, A. L.; Bai, Z. T.; Zhang, X.; Zheng, X.; Liu, Z.; Gao, F. L. An NIR-driven upconversion/C_3N_4/CoP photocatalyst for efficient hydrogen production by inhibiting electron-hole pair recombination for Alzheimer's disease therapy. *ACS Nano* **2023**, *17*, 2222–2234.

[4] Yin, Y. M.; Chen, G. F.; Gong, L.; Ge, K. Z.; Pan, W. Z.; Li, N.; Machuki, J. O.; Yu, Y. Y.; Geng, D. Q.; Dong, H. F. et al. DNAzyme-powered three-dimensional DNA walker nanoprobe for detection amyloid β-peptide oligomer in living cells and *in vivo*. *Anal. Chem.* **2020**, *92*, 9247–9256.

[5] Wu, Y. C.; Bogale, T. A.; Koistinaho, J.; Pizzi, M.; Rolova, T.; Bellucci, A. The contribution of *β*-amyloid, Tau and *α*-synuclein to blood-brain barrier damage in neurodegenerative disorders. *Acta Neuropathol.* **2024**, *147*, 39.

[6] Zhu, C. L.; Yang, Y. H.; Li, X. W.; Chen, X. Y.; Lin, X. C.; Wu, X. P. Develop potential multi-target drugs by self-assembly of quercetin with amino acids and metal ion to achieve significant efficacy in anti-Alzheimer's disease. *Nano Res.* **2022**, *15*, 5173–5182.

[7] Ceyzériat, K.; Zilli, T.; Millet, P.; Frisoni, G. B.; Garibotto, V.; Tournier, B. B. Learning from the past: A review of clinical trials targeting amyloid, tau and neuroinflammation in Alzheimer's disease. *Curr. Alzheimer Res.* **2020**, *17*, 112–125.

[8] Golde, T. E.; DeKosky, S. T.; Galasko, D. Alzheimer's disease: The right drug, the right time. *Science* **2018**, *362*, 1250–1251.

[9] Congdon, E. E.; Sigurdsson, E. M. Tau-targeting therapies for Alzheimer disease. *Nat. Rev. Neurol.* **2018**, *14*, 399–415.

[10] El Mammeri, N.; Dregni, A. J.; Duan, P.; Wang, H. K.; Hong, M. Microtubule-binding core of the tau protein. *Sci. Adv.* **2022**, *8*, eabo4459.

[11] Christensen, C. S.; Wang, S. A.; Li, W. S.; Yu, D. Y.; Li, H. J. Structural variations of prions and prion-like proteins associated with neurodegeneration. *Curr. Issues Mol. Biol.* **2024**, *46*, 6423–6439.

[12] Sun, X. R.; Ruan, H. T.; Liu, Q. D.; Cao, S. L.; Jing, Q.; Xu, Y. R.; Xiong, L. Z.; Cui, W. G.; Li, C. Targeted regulation of neuroinflammation via nanobiosignaler for repairing the central nerve system injuries. *Nano Res.* **2023**, *16*, 2938–2948.

[13] Prater, K. E.; Green, K. J.; Mamde, S.; Sun, W.; Cochoit, A.; Smith, C. L.; Chiou, K. L.; Heath, L.; Rose, S. E.; Wiley, J. et al. Human microglia show unique transcriptional changes in Alzheimer's disease. *Nat. Aging* **2023**, *3*, 894–907.

[14] Salter, M. W.; Stevens, B. Microglia emerge as central players in brain disease. *Nat. Med.* **2017**, *23*, 1018–1027.

[15] Hu, X. M.; Leak, R. K.; Shi, Y. J.; Suenaga, J.; Gao, Y. Q.; Zheng, P.; Chen, J. Microglial and macrophage polarization-new prospects for brain repair. *Nat. Rev. Neurol.* **2015**, *11*, 56–64.

[16] Leng, F. D.; Edison, P. Neuroinflammation and microglial activation in Alzheimer disease: Where do we go from here. *Nat. Rev. Neurol.* **2021**, *17*, 157–172.

[17] Liu, H. H.; Han, Y. B.; Wang, T. T.; Zhang, H.; Xu, Q.; Yuan, J. X.; Li, Z. Targeting microglia for therapy of Parkinson's disease by using biomimetic ultrasmall nanoparticles. *J. Am. Chem. Soc.* **2020**, *142*, 21730–21742.

[18] Li, T. Z.; Hou, X. Y.; Qi, Y.; Duan, X. H.; Yan, P. C.; Zhu, H. R.; Xie, Z. J.; Zhang, H. Nanomaterials for neurodegenerative diseases: Molecular mechanisms guided design and applications. *Nano Res.* **2022**, *15*, 3299–3322.

[19] Fu, P. P.; Xia, Q. S.; Sun, X.; Yu, H. T. Phototoxicity and environmental transformation of polycyclic aromatic hydrocarbons (PAHs)-light-induced reactive oxygen species, lipid peroxidation, and DNA damage. *J. Environ. Sci. Health Part C* **2012**, *30*, 1–41.

[20] Ren, C. X.; Li, D. D.; Zhou, Q. X.; Hu, X. G. Mitochondria-targeted TPP-MoS_2 with dual enzyme activity provides efficient neuroprotection through M1/M2 microglial polarization in an Alzheimer's disease model. *Biomaterials* **2020**, *232*, 119752.

[21] Boyetey, M. J. B.; Choi, Y.; Lee, H. Y.; Choi, J. Nanotechnology-based delivery of therapeutics through the intranasal pathway and the blood-brain barrier for Alzheimer's disease treatment. *Biomater. Sci.* **2024**, *12*, 2007–2018.

[22] Li, L. Q.; Zhang, W. Y.; Cao, H. Y.; Fang, L. M.; Wang, W. J.; Li, C. Z. L.; He, Q. B.; Jiao, J. W.; Zheng, R. X. Nanozymes in Alzheimer's disease diagnostics and therapy. *Biomater. Sci.* **2024**, *12*, 4519–4545.

[23] Ma, X. X.; Hao, J. N.; Wu, J. R.; Li, Y. H.; Cai, X. J.; Zheng, Y. Y. Prussian blue nanozyme as a pyroptosis inhibitor alleviates neurodegeneration. *Adv. Mater.* **2022**, *34*, 2106723.

[24] Wang, Y. H.; Liang, Z. H.; Liang, Z. Y.; Lv, W. F.; Chen, M.; Zhao, Y. Advancements of Prussian blue-based nanoplatforms in biomedical fields: Progress and perspectives. *J. Control. Release* **2022**, *351*, 752–778.

[25] Feng, L. S.; Dou, C. R.; Xia, Y. G.; Li, B. H.; Zhao, M. Y.; El-Toni, A. M.; Atta, N. F.; Zheng, Y. Y.; Cai, X. J.; Wang, Y. et al. Enhancement of nanozyme permeation by endovascular interventional treatment to prevent vascular restenosis via macrophage polarization modulation. *Adv. Funct. Mater.* **2020**, *30*, 2006581.

[26] Wu, Q. H.; Zhou, Y.; Yan, J.; Li, X. D.; Meng, F. H.; Wang, B.; Yin, L. C. Biomimetic nanocomplexes orchestrate post-stroke cerebral microenvironment via microglia-targeted siRNA delivery. *Nano Today* **2024**, *58*, 102444.

[27] Zhou, Y.; Liang, Q. J.; Wu, X. J.; Duan, S. Z.; Ge, C. L.; Ye, H.; Lu, J. H.; Zhu, R. Y.; Chen, Y. B.; Meng, F. H. et al. siRNA delivery against myocardial ischemia reperfusion injury mediated by reversibly camouflaged biomimetic nanocomplexes. *Adv. Mater.* **2023**, *35*, 2210691.

[28] Peng, J. R.; Dong, M. L.; Ran, B.; Li, W. T.; Hao, Y.; Yang, Q.; Tan, L. W.; Shi, K.; Qian, Z. Y. "One-for-all"-type, biodegradable Prussian blue/manganese dioxide hybrid nanocrystal for trimodal imaging-guided photothermal therapy and oxygen regulation of breast cancer. *ACS Appl. Mater. Interfaces* **2017**, *9*, 13875–13886.

[29] Wang, C.; Zhang, M. L.; Bai, L. P.; Gai, P. P.; Li, F. Light-driven self-cascade peroxidase-like nanozymes without exogenous H_2O_2. *Anal. Chem.* **2023**, *95*, 7014–7020.

[30] Jin, Y.; Peng, Q. C.; Xie, J. W.; Li, K.; Zang, S. Q. Photo-activated circularly polarized luminescence film based on aggregation-induced emission copper (I) cluster-assembled materials. *Angew. Chem.* **2023**,

135, e202301000.
[31] Chou, C. H.; Yang, C. R. Neuroprotective studies of evodiamine in an okadaic acid-induced neurotoxicity. *Int. J. Mol. Sci.* **2021**, *22*, 5347.
[32] Zhao, J. H.; Yin, F. C.; Ji, L. M.; Wang, C.; Shi, C. J.; Liu, X. C.; Yang, H. L.; Wang, X. B.; Kong, L. Y. Development of a tau-targeted drug delivery system using a multifunctional nanoscale metal-organic framework for Alzheimer's disease therapy. *ACS Appl. Mater. Interfaces* **2020**, *12*, 44447–44458.
[33] Pan, Y. M.; Zhang, Y. L.; Liu, N.; Lu, W. Y.; Yang, J. X.; Li, Y.; Liu, Z. W.; Wei, Y. H.; Lou, Y.; Kong, J. Vitamin D attenuates Alzheimer-like pathology induced by Okadaic acid. *ACS Chem. Neurosci.* **2021**, *12*, 1343–1350.
[34] Cai, X. J.; Gao, W.; Ma, M.; Wu, M. Y.; Zhang, L. L.; Zheng, Y. Y.; Chen, H. R.; Shi, J. L. A Prussian blue-based core-shell hollow-structured mesoporous nanoparticle as a smart theranostic agent with ultrahigh pH-responsive longitudinal relaxivity. *Adv. Mater.* **2015**, *27*, 6382–6389.
[35] Dumont, M. F.; Hoffman, H. A.; Yoon, P. R. S.; Conklin, L. S.; Saha, S. R.; Paglione, J. P.; Sze, R. W.; Fernandes, R. Biofunctionalized gadolinium-containing prussian blue nanoparticles as multimodal molecular imaging agents. *Bioconjugate Chem.* **2014**, *25*, 129–137.
[36] Cafun, J. D.; Champion, G.; Arrio, M. A.; dit Moulin, C. C.; Bleuzen, A. Photomagnetic CoFe Prussian blue analogues: Role of the cyanide ions as active electron transfer bridges modulated by cyanide-alkali metal ion interactions. *J. Am. Chem. Soc.* **2010**, *132*, 11552–11559.
[37] Wojdeł, J. C.; Bromley, S. T. Band gap variation in Prussian blue via cation-induced structural distortion. *J. Phys. Chem. B* **2006**, *110*, 24294–24298.
[38] Jomova, K.; Vondrakova, D.; Lawson, M.; Valko, M. Metals, oxidative stress and neurodegenerative disorders. *Mol. Cell. Biochem.* **2010**, *345*, 91–104.
[39] Pan, S. Y.; Sun, Z. W.; Zhao, B.; Miao, L. Q.; Zhou, Q. F.; Chen, T. F.; Zhu, X. Q. Therapeutic application of manganese-based nanosystems in cancer radiotherapy. *Biomaterials* **2023**, *302*, 122321.
[40] Tian, R. Z.; Ma, H. Y.; Ye, W.; Li, Y. J.; Wang, S. P.; Zhang, Z. R.; Liu, S. D.; Zang, M. S.; Hou, J. X.; Xu, J. Y. et al. Se-containing MOF coated dual-Fe-atom nanozymes with multi-enzyme cascade activities protect against cerebral ischemic reperfusion injury. *Adv. Funct. Mater.* **2022**, *32*, 2204025.
[41] Liu, C. P.; Wu, T. H.; Liu, C. Y.; Chen, K. C.; Chen, Y. X.; Chen, G. S.; Lin, S. Y. Self-supplying O_2 through the catalase-like activity of gold nanoclusters for photodynamic therapy against hypoxic cancer cells. *Small* **2017**, *13*, 1700278.
[42] Jiang, X. X.; Liu, K.; Li, Q.; Liu, M.; Yang, M. H.; Chen, X. B-Doped core-shell Fe@BC nanozymes: Active site identification and bacterial inhibition. *Chem. Commun.* **2021**, *57*, 1623–1626.
[43] Kim, D.; Su, J.; Cotman, C. W. Sequence of neurodegeneration and accumulation of phosphorylated tau in cultured neurons after okadaic acid treatment. *Brain Res.* **1999**, *839*, 253–262.
[44] Kamat, P. K.; Nath, C. Okadaic acid: A tool to study regulatory mechanisms for neurodegeneration and regeneration in Alzheimer's disease. *Neural Regen. Res.* **2015**, *10*, 365–367.
[45] Shi, Y.; Bu, W. Z.; Chu, D. C.; Lin, W. Z.; Li, K.; Huang, X. P.; Wang, X. L.; Wu, Y.; Wu, S.; Li, D. D. et al. Rescuing nucleus pulposus cells from ROS toxic microenvironment via mitochondria-targeted carbon dot-supported Prussian blue to alleviate intervertebral disc degeneration. *Adv. Healthc. Mater.* **2024**, *13*, 2303206.
[46] Bartsch, T.; Döhring, J.; Rohr, A.; Jansen, O.; Deuschl, G. CA1 neurons in the human hippocampus are critical for autobiographical memory, mental time travel, and autonoetic consciousness. *Proc. Natl. Acad. Sci. USA* **2011**, *108*, 17562–17567.
[47] Wolf, S. A.; Boddeke, H. W. G. M.; Kettenmann, H. Microglia in physiology and disease. *Annu. Rev. Physiol.* **2017**, *79*, 619–643.